

Deep learning Inversion of Seismic Data

Shucaí Li, Bin Liu, Yuxiao Ren, Yangkang Chen, Senlin Yang, Yunhai Wang, *Member, IEEE*,
and Peng Jiang, *Member, IEEE*

Abstract—In this paper, we propose a new method to tackle the mapping challenge from time-series data to spatial image in the field of seismic exploration, i.e., reconstructing the velocity model directly from seismic data by deep neural networks (DNNs). The conventional way to address this ill-posed seismic inversion problem is through iterative algorithms, which suffer from poor nonlinear mapping and strong non-uniqueness. Other attempts may either import human intervention errors or underuse seismic data. The challenge for DNNs mainly lies in the weak spatial correspondence, the uncertain reflection-reception relationship between seismic data and velocity model as well as the time-varying property of seismic data. To approach these challenges, we propose an end-to-end Seismic Inversion Networks (SeisInvNet for short) with novel components to make the best use of all seismic data. Specifically, we start with every seismic trace and enhance it with its neighborhood information, its observation setup and global context of its corresponding seismic profile. Then from enhanced seismic traces, the spatially aligned feature maps can be learned and further concatenated to reconstruct velocity model. In general, we let every seismic trace contribute to the reconstruction of the whole velocity model by finding spatial correspondence. The proposed SeisInvNet consistently produces improvements over the baselines and achieves promising performance on our proposed SeisInv dataset according to various evaluation metrics, and the inversion results are more consistent with the target from the aspects of velocity value, subsurface structure and geological interface. In addition to the superior performance, the mechanism is also carefully discussed, and some potential problems are identified for further study.

Index Terms—Seismic inversion, Deep neural networks.

I. INTRODUCTION

Seismic exploration is often used to map the structure of subsurface formations based on the propagation of seismic wave in the earth. It can estimate the physical properties of the Earth's subsurface mainly from reflected or refracted seismic waves. Since seismic exploration is capable of detecting target features from a large to small scale, it plays an important role in delineation of near-surface geology for engineering purpose, hydrocarbon exploration as well as the Earth's crustal structure investigation. Usually, artificial sources of energy are required and a series of receivers are placed on the surface to record seismic waves (as illustrated in Fig. 1). One major outcome of processing the recorded data is to reconstruct the underground velocity model, namely seismic velocity inversion, which has a substantial impact on the accuracy of locating and imaging target bodies. Recently, by using full waveform information of seismic data, full waveform inversion (FWI) is now one of

the most appealing methods to reconstruct the velocity model with high accuracy and resolution [1]–[3].

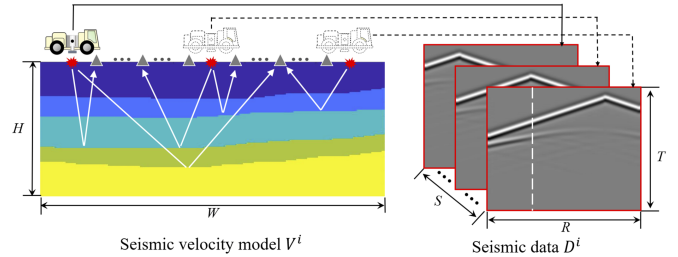


Fig. 1. Illustration of seismic exploration, which maps seismic velocity model (spatial image) to time-series seismic data. Seismic data is composed of seismic profiles denoted by red border. Each seismic profile corresponds to seismic data recorded by all receivers from a seismic source. The white dashed line on seismic profile indicates a seismic trace recorded by a single receiver.

FWI was firstly proposed in the early 1980s. It reconstructs the velocity model by iteratively minimizing the difference between seismic data and synthetic data in a least-squares sense [4]–[6]. Conventional FWI uses gradient-based solvers to update the model parameters, and the gradient is normally calculated through backward wavefield propagation of data residuals based on adjoint-state methods [7], [8]. However, seismic velocity estimation from observed signals is a highly nonlinear process, so that iterative linear algorithm usually requires a good starting model to avoid local minimum. Moreover, FWI also faces severe non-uniqueness because of inadequate observation or observation data contaminated with noise. Facing these non-linearity and non-uniqueness issues in conventional FWI, geophysicists have proposed many improvements, such as the multiscale strategy [9]–[12], processing of seismic data in other domain [13], [14], etc.

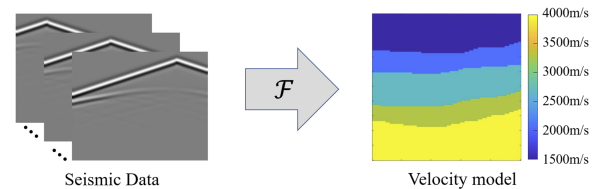


Fig. 2. Task definition. DNNs based seismic inversion is to learn the function \mathcal{F} that maps seismic data to its corresponding velocity model.

Recently, Deep Neural Networks (DNNs) have demonstrated remarkable ability to approximate nonlinear mapping function between various data domains [15], such as, images and label maps (e.g. [16], [17]), images and texts (e.g. [18], [19]) and different types of images (e.g. [20], [21]). Especially for inverse problems, such as model/image reconstruction (e.g. [22], [23]), image super-resolution (e.g. [24]–[26]), real-world photo synthesis (e.g. [27], [28]), etc. These state-of-the-art developments bring new perspectives for seismic inversion and

S. Li, B. Liu, Y. Ren, S. yang, Y. Wang and P. Jiang are with Shandong University, China. (Emails: lishucal@sdu.edu.cn; liubin0635@163.com; ryxchina@gmail.com; yangsenlin@mail.sdu.edu.cn; cloudseawang@gmail.com and sdujump@gmail.com). Y. Chen is with Zhejiang University, China. (Email: yangkang.chen@zju.edu.cn)

velocity model reconstruction. DNNs based seismic inversion is to learn the mapping function \mathcal{F} from seismic data to velocity model, as illustrated in Fig. 2. So far, some works have already made progress on this task. Moseley *et al.* [29] achieved 1D velocity model inversion by WaveNet [30] after depth-to-time conversion of the velocity profile. Araya-Polo *et al.* [31] use Convolutional Neural Networks (CNNs) to reconstruct velocity model from a semblance cube calculated from raw data. These two works may introduce artifacts because of the human intervention in seismic data processing. Other than data processing, Wu *et al.* [32] proposed InversionNet to build the mapping from raw seismic data to the corresponding velocity model directly, following the autoencoder architecture to decode the velocity model from an embedding vector which encodes the whole seismic data. Since data is extremely condensed in the embedding vector, decoded velocity model may lose details.

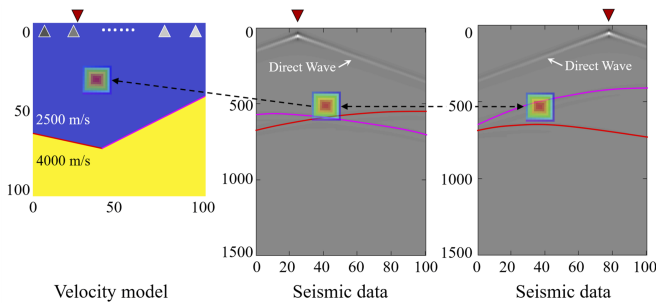


Fig. 3. Velocity model and its corresponding seismic profiles. Left: the velocity model with one downward and upward interface; Middle: the profile of seismic data based on one shot in location 25; Right: the profile of seismic data based on one shot in location 75. The red and purple curves on the seismic profiles denote signals from the downward part and upward part of the interface respectively. Notice that the squares with jet color indicate patches all lie on the same relative positions. The patch on the left seismic profile contains reflected signals from both upward and downward parts of interface while the patch on the right seismic profile only contains signals from the upward part. However, the patch on the velocity model does not have any information about the interface. That is, either spatial correspondence between the velocity model and the seismic profiles or between different seismic profiles are not aligned.

Inspired by recent progress, and to avoid potential problems of the works mentioned above, we further analyze the characteristics of the DNNs based seismic inversion task. In general, the characteristics mainly lie in three aspects. Firstly, the spatial correspondence between raw time-series signals (seismic data) and seismic images (velocity model) is weak, especially for reflected seismic signals. As illustrated in Fig. 3, for the position where exists a reflected wave on seismic profile, the corresponding position on the velocity model may not contain any interface and vice versa. This weak spatial correspondence issue was also mentioned in [33]. Secondly, considering the complexity of underground structure in various velocity models, for reflected seismic signals received by one receiver from one source (i.e., seismic trace), the corresponding interfaces which cause the reflections in velocity model are uncertain. In this paper, we use the term uncertain reflection-reception relationship to refer to this characteristic. Thirdly, in raw seismic data, the recorded seismic wave gradually weakens as time goes by. That is, seismic data is of time-varying property, which makes seismic pattern hard to capture with

fixed kernel. All these characteristics pose a great challenge for DNNs, especially for CNNs with spatial correspondence and weight sharing properties.

To address these unique and intrinsic characteristics, in this paper we propose an end-to-end DNN with novel components called SeisInvNet. The idea is that we firstly learn feature map spatially aligned to the velocity model from each seismic trace, after building the spatial correspondence, the velocity model could be reconstructed from the learned feature maps effortlessly. Specifically, considering the uncertain reflection-reception relationship, we enforce each seismic trace to learn a feature map with information corresponding to the whole velocity model regardless actual relationship between each seismic trace and velocity model. Then from all the feature maps, we reconstruct velocity model by CNNs. Thus, after training, the information in each feature map will spatially align to the velocity model. Since each seismic trace has its sensitivity region, so the feature map from different seismic trace will contain knowledge to reconstruct different part of velocity model. We learn spatially aligned feature map by fully connected layers which could deal with the uncertainty and time-varying properties of seismic data. In this way, we solve the challenge of uncertain reflection-reception relationship, build the spatial correspondence and meanwhile get rid of the time-varying problem.

Moreover, in seismic exploration, seismic trace is often observed along with its neighborhood traces to identify the local structure and all seismic traces combined together to deduce the global context. Thus, before learning the feature map, we enhance each seismic trace with some auxiliary knowledge from several neighborhood traces and the whole profile. Since we use each enhanced seismic trace as actual input rather than the large raw seismic data, our SeisInvNet will save a lot of parameters to optimize. Furthermore, all the mentioned operations could be trained end-to-end. In general, we make the best use of all seismic data and let every seismic trace contribute to the reconstruction of the whole velocity model by finding spatial correspondence.

We carry out experiments on a self-proposed SeisInv dataset. From comprehensive comparisons, our SeisInvNet has demonstrated superior performance against all the baseline models consistently. Our inversion results are more consistent with the ground truth from the aspects of velocity value, sub-surface structure and geological interface. Further, we study the mechanism of SeisInvNet by visualization and statistics analysis.

Major contributions reside in the following aspects.

- We make an in-depth analysis on the problem of DNNs based seismic inversion.
- We design SeisInvNet with novel and efficient components to take full advantage of all the seismic data.
- We demonstrate superior performance against all the baseline models on proposed SeisInv dataset.
- We provide comprehensive mechanism studies.

II. RELATED WORKS

Several works have tried seismic inversion problems by DNNs in various ways, which can be concluded as follows:

A. Data Preprocessing Based Seismic Inversion

To make raw seismic data and the corresponding velocity model spatially aligned, data preprocessing is always an option to consider, though at the risk of introducing human assumptions. Moseley *et al.* [29] make single-receiver recorded signal spatially aligned to the model by the standard 1D time-to-depth conversion before doing 1D velocity model inversion by WaveNet [30]. Araya-Polo *et al.* [31] transfer raw seismic data into a velocity related feature cube by normal moveout correction of common midpoint gather data [34] before applying CNNs.

B. Encoder-Decoder Networks Based Seismic Inversion

When images have specific fixed structures or patterns, they can be reconstructed without providing low-level information such as spatial correspondence. In this case, even discarding spatial information and compressing original data to a 1D embedding vector, we can still get desired output without losing much information. This process can be achieved by the Encoder-Decoder Networks (autoencoder for short) that encoder compresses input to the embedding vector while from which decoder reconstructs the output. This kind of autoencoder has been widely utilized for tasks on the aligned face dataset, such as face generation [35], [36]. According to their experiments, the embedding vector contains high-level information such as expression, gender, age, etc. It's also fit the human behaviors that we can draw the portrait only given some high-level semantic descriptions. However, when it comes to more complex images, low-level information will have critic importance. For example, medical image semantic segmentation methods such as U-Net [23], [37] concatenate low-level features on the output of deep layers by shortcuts to compensate details of the results, but they only work on data where input and output are spatially aligned.

For seismic inversion problem where input and output are not spatially aligned, Encoder-Decoder Networks can still be applied to extract the embedding vector. This way was adopted by Wu *et al.* [32] to propose InversionNet, which works well on velocity model with relatively fixed patterns (horizontal interfaces and dipping faults) according to their paper. However, when velocity models contain a large number of small structures, embedding vector may fail to preserve all the details. As Fig. 8 demonstrated, autoencoder inverted results sometimes lose details in our implementation.

C. Other related work

Multi-Layer Perceptron Neural Networks (MLPs) with fully connected layers is the most direct way to construct a mapping between data of weak spatial correspondence. The output of each fully connected layers will depend on all the input value thus information carried by seismic data could be best captured. However, in this way, the computation and space complexity is proportional to the square of data dimension. Dahlke *et al.* [33] developed a probabilistic model to indicate the existence of faults in the 2D velocity model using MLPs while Araya-Polo *et al.* [38] extend this method to the 3D

case. To reduce computation complexity, they have to first convert the model to the low dimensional pixel or voxel grid, so that the faults could only be coarsely identified. In addition to reflected seismic waves, transmitted waves can also be used to reconstruct velocity models. For example, based on prestack multi-shot seismic traces of transmitted wave, Wang *et al.* [39] achieved satisfactory inversion results using fully convolutional networks.

III. METHODOLOGY AND IMPLEMENTATION

A. Methodology

In order to better define the problem, let us firstly introduce some notations. We have N velocity model $V^i, i \in N$ and the corresponding N seismic data $D^i, i \in N$. Each velocity model V^i is of size $[H, W]$, while each seismic data D^i is of size $[S, T, R]$. Here, H and W denote the height and width of the velocity model while S , R and T denote the number of seismic sources, receivers and time steps respectively. Each seismic data D^i can be treated as $S \times R$ single seismic trace $D^i_{s,r}$ of dimension T while all the single seismic traces from the same source form the seismic profile $D^i_{s,\cdot}$ of dimension $[T, R]$. Visual illustration of these notations is shown in Fig. 1.

In this work, we intend to learn the mapping \mathcal{F} from seismic data D^i to velocity model V^i directly, namely seismic inversion, by DNNs with parameters θ :

$$\mathcal{F}(D^i, \theta) \rightarrow V^i. \quad (1)$$

In general, for an image to image mapping, CNNs are preferred. However, in our case, directly using CNNs may not be the optimal choice. There are two unique characteristics of the mapping between seismic data and velocity model: (1) Weak spatial correspondence. The interface in velocity model and the corresponding pattern in seismic data have weak spatial correspondence. (2) Uncertain reflection-reception relationship between seismic data and velocity model. For a seismic trace, the corresponding interfaces which cause the reflected signals are uncertain in different velocity models. These characteristics will be problematic for the spatial correspondence property of CNNs. Besides, there is another potential problem that seismic wave weakens gradually as time goes by, which may pose another challenge for the weight sharing property of CNNs. As stated in Sec. II, one possible way of using CNNs regardless of the spatial correspondence and weight sharing issue is by Encoder-Decoder Networks, which condense seismic data into a 1D embedding vector and abandon its spatial information. As demonstrated in Fig. 7, this way sometimes leads to inaccurate inversion of velocity models.

Instead, in this work, we intend to take full use of seismic data without much loss of information by DNNs. Consequently, we have the following methodology. In general, we firstly learn feature map $f^i_{s,r}$ contains information spatially aligned to the velocity model V^i from each seismic trace $D^i_{s,r}$, and then we regress the velocity model V^i from all the spatially aligned feature maps $[f^i_{s,r} : s \in S, r \in R]$. In practice, because the uncertain relationship between seismic trace and interfaces in velocity model, regardless of actual relationship, we choose to let each seismic trace learn the feature map which

implies knowledge corresponding to the whole velocity model. After training, the spatial correspondence between feature map and velocity model will be built, and feature map from different seismic trace will provide knowledge to reconstruct different part of velocity model since each seismic trace has its sensitivity region. However, this mapping is ambiguous since different seismic observation setup and underground geology conditions may result in the same seismic trace records, i.e., $D_{\hat{s},\hat{r}}^i = D_{\bar{s},\bar{r}}^i$, $\hat{s} \neq \bar{s}$, $\hat{r} \neq \bar{r}$. To reduce the uncertainty and enrich the knowledge, for each seismic trace data $D_{s,r}^i$ recorded by single receiver r and single shot s , we enhance it by encoding its neighborhood information $\mathcal{N}(D_{s,:}^i)_r$, its observation setup $S(D_{s,r}^i)$ and global context of its s -th profile $\mathcal{G}(D_{s,:}^i)$ that we replace $D_{s,r}^i$ with an embedding vector $\mathbf{E}_{s,r}^i$ that

$$\mathbf{E}_{s,r}^i = [\mathcal{N}(D_{s,:}^i)_r, S(D_{s,r}^i), \mathcal{G}(D_{s,:}^i)]. \quad (2)$$

Compared with $D_{s,r}^i$, $\mathbf{E}_{s,r}^i$ contains much more rich knowledge to generate spatially aligned and unambiguous feature map $f_{s,r}^i$. Intuitively speaking, neighborhood information would help networks get aware of the pattern of local seismic data, such as existence and direction of reflected wave; observation setup would make information more distinguishable and less ambiguous by telling how each seismic trace data is recorded; and global context would supplement global information, such as velocity distribution and number of interfaces.

Given these information, it's feasible to generate spatially aligned feature $f_{s,r}^i$ from $\mathbf{E}_{s,r}^i$ that

$$\mathcal{F}_1(\mathbf{E}_{s,r}^i, \theta_1) = f_{s,r}^i, \quad (3)$$

where \mathcal{F}_1 and θ_1 are feature generating function and its parameters. Collecting all the feature maps, we have $\mathbf{F}^i = [f_{s,r}^i : s \in S, r \in R]$ with dimension $[S \times R, h, w]$.

Finally, we could regress velocity model V^i from \mathbf{F}^i with commonly used CNNs since we have built the spatial correspondence between \mathbf{F}^i and V^i that

$$\mathcal{F}_2(\mathbf{F}^i, \theta_2) = V^i, \quad (4)$$

where \mathcal{F}_2 and θ_2 are velocity model regressing function and its parameters.

In a nutshell, in our method, we build the mapping \mathcal{F} by

$$\mathcal{F} : D^i \xrightarrow{\mathcal{N}, S, \mathcal{G}} \mathbf{E}^i \xrightarrow{\mathcal{F}_1} \mathbf{F}^i \xrightarrow{\mathcal{F}_2} V^i. \quad (5)$$

In the following, we will describe how to implement \mathcal{N} , \mathcal{G} , \mathcal{F}_1 , \mathcal{F}_2 by DNNs respectively.

B. Implementation

Fig. 4 has illustrated our proposed SeisInvNet which has four components.

1) *Embedding Encoder*: Embedding Encoder generates embedding vectors which contain neighborhood information, observation setup and global context.

We extract neighborhood information by a shadow CNNs (\mathcal{N}) on seismic profile $D_{s,:}^i$. The output of \mathcal{N} has the same dimension as the input, but the value in each position of $\mathcal{N}(D_{s,:}^i)$ contains its neighborhood information rather than the raw value. Consequently, the column $\mathcal{N}(D_{s,:}^i)_r$ (of dimension

T) contains the neighborhood information of seismic trace $D_{s,r}^i$. As for observation setup, S transforms the position of receiver r and source s to the one-hot vector. Since $s \in [1, S]$ and $r \in [1, R]$, so that the observation setup $S(D_{s,r}^i)$ is a vector of dimension $S + R$. Global context is a vector of dimension C extracted from seismic profile $D_{s,:}^i$ by an encoder \mathcal{G} . The encoder \mathcal{G} is also implemented by CNNs, which constantly compresses data by convolution operation until the spatial dimension vanished.

Finally, as Eq. 2, we collect $\mathcal{N}(D_{s,:}^i)_r$, $S(D_{s,r}^i)$ and $\mathcal{G}(D_{s,:}^i)$ to form an embedding vector $\mathbf{E}_{s,r}^i$ of dimension $T + S + R + C$ which replaces the original T dimensional seismic trace $D_{s,r}^i$. Sometimes we will refer $\mathbf{E}_{s,r}^i$ as enhanced seismic trace. It's worth to note that all CNNs based \mathcal{N} and \mathcal{G} are weight sharing over all the applied data.

2) *Spatially Aligned Feature Generator*: Given the $S \times R$ embedding vectors \mathbf{E}^i , we firstly further condense them to vectors of size $h \times w$ using MLPs (\mathcal{F}_1) with several fully connected layers (including activation and norm operations), then reshape each vector to feature map $f_{s,r}^i$ of size $[h, w]$. Since the embedding vector has much less dimension than the raw seismic data, the mapping to feature map is acceptable for the fully connected layers. We design Generator to output feature map with the same dimension ratio as velocity model. From these feature maps, velocity model will be reconstructed directly. Thus, after training, every part of feature map will imply knowledge in the corresponding part of velocity model, so feature map is spatially aligned to velocity model. Besides, feature map $f_{s,r}^i$ originated from different source s and receiver r would focus on the different part of velocity model that each feature map has its sensitivity region. We show feature maps in Sec. IV-F to verify the above statements.

3) *Velocity Model Decoder*: Velocity Model Decoder collects all $S \times R$ feature maps \mathbf{F}^i from which knowledge is decoded to regress velocity model V^i (of size $[1, H, W]$) by CNNs (\mathcal{F}_2) with several convolutional layers (including activation and norm operations). During training, Velocity Model Decoder randomly throw away several feature maps (dropout) to make Decoder not only depend on certain feature maps when reconstructing velocity model, which improves its robustness and prevents over-fitting.

4) *Loss Function*: What results look like is mainly depended on how the loss function is designed. For image regression and reconstruction problems, L_1 or L_2 norm is the most commonly used metric to define the loss function. However, these metrics treat each position of image individually which make networks hard to capture local structures and details, such as edges and corners. In experiments of Wang *et al.* [40], with the same L_2 score, processed images show dramatic difference that L_2 is inconsistent with human perception.

Local structures and details are important factors to concern in reconstructing seismic velocity models [41]–[43]. To measure these factors, Structural Similarity Index (*SSIM*) proposed by Wang *et al.* [40] is the most commonly used metric which computes the statistics difference between two corresponding

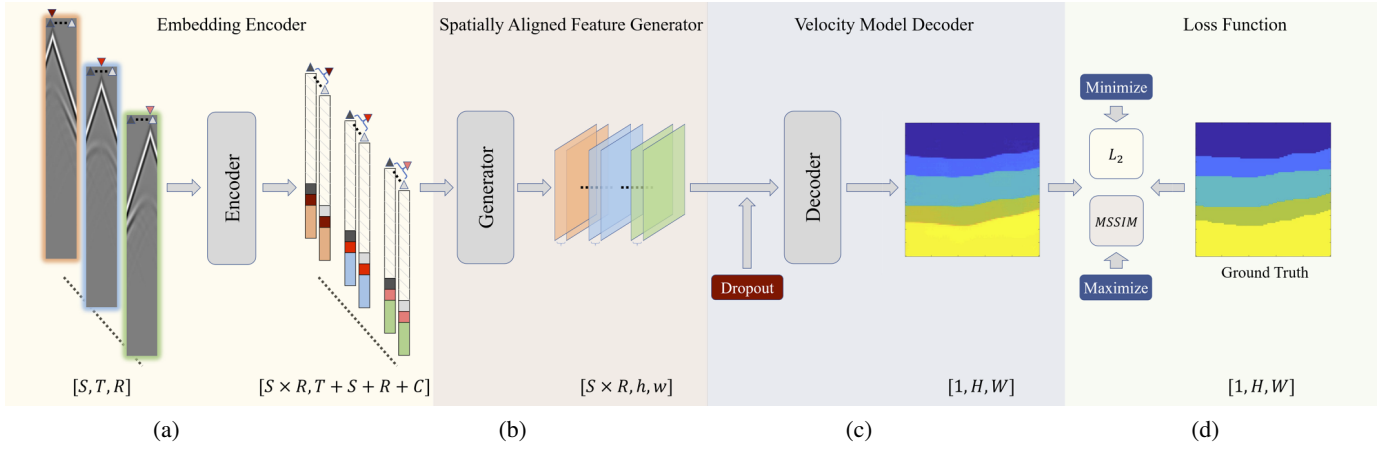


Fig. 4. Visualization of SeisInvNet framework. Given the seismic data (\blacktriangledown to \blacktriangleleft indicate data by different sources while \blacktriangle to \blacktriangleright indicate data recorded by different receivers. To save space, data is not visualized in its original scale.), (a) *Embedding Encoder* replaces each original seismic trace $D_{s,r}^i$ by an embedding vector $\mathbf{E}_{s,r}^i$ which composes of neighborhood information $\mathcal{N}(D_{s,r}^i)_r$ (indicated by \square), observation setup $S(D_{s,r}^i)$ (indicated by squares, such as \blacksquare and \blacklozenge), and global context $\mathcal{G}(D_{s,r}^i)$ of corresponding seismic profile (indicated by rectangles, such as \blacksquare , \blacksquare and \blacksquare); (b) *spatially aligned feature Generator* transforms each embedding vector to a feature map whose information is spatially aligned to the velocity model; (c) *Velocity Model Decoder* collects all the feature maps from which knowledge is decoded to regress velocity model. (d) We optimize parameters of Encoder, Generator, and Decoder by minimizing L_2 and maximizing $MSSIM$ metrics to make output more closed to the Ground Truth. Check Sec. III-B for the details.

windows in predict and target. $SSIM$ is defined as

$$SSIM(x, y) = \frac{(2\mu_x\mu_y + c_1)(2\sigma_{xy} + c_2)}{(\mu_x^2 + \mu_y^2 + c_1)(\sigma_x^2 + \sigma_y^2 + c_2)}, \quad (6)$$

where x and y are two corresponding windows while c_1 and c_2 are variables to stabilize the division. $SSIM$ score ranges from 0 to 1, and it reaches its maximum when information in two windows are entirely the same.

Accordingly, apart from minimizing norm metric, in this work we will simultaneously maximize $SSIM$ metric. Specifically, we apply L_2 norm and Multiscale Structural Similarity ($MSSIM$) [44] to compute the loss \mathcal{L}_i for each data pair that

$$\mathcal{L}_i(\bar{V}^i, V^i) = \sum_{k=0}^{H \times W} \|\bar{V}_k^i - V_k^i\|_2 - \sum_{r \in R} \sum_{k=0}^{H \times W} \lambda_r SSIM(\bar{V}_{x(k,r)}^i, V_{y(k,r)}^i), \quad (7)$$

where \bar{V}^i and V^i are the inversion result and ground truth respectively for i -th data pair, $x_{(k,r)}$ and $y_{(k,r)}$ are the two corresponding windows centered in k of size r . We carry out $SSIM$ on total R different scales, for each scale r we have a weight λ_r to control its importance.

IV. EXPERIMENTS

A. Dataset preparation

In this section, we give a detailed description of how the dataset is prepared. Our dataset has 12,000 different velocity model and the corresponding synthetic seismic data pairs. Since this dataset is mainly for inversion problem, we name our dataset SeisInv dataset. Consequently, synthetic seismic data is the input while the velocity model is the ground truth.

In this work, velocity models are designed to have horizontally layered structures with several small ups and downs randomly distributed along the interfaces. In general, the velocity models in our dataset can be divided into four subsets, namely type I, II, III and IV respectively, according to the number of underground interfaces. In each category,

3,000 different models are designed by firstly generating the geology interfaces and then filling the layers between two adjacent interfaces with a constant velocity value randomly selected from [1500, 4000]. According to the statistics of actual underground geological conditions, the deeper stratum tends to have a larger seismic velocity. Consequently, we let the velocity value monotone increase with stratum and have the difference over 300m/s for adjacent geological layers. The overall statistics including mean, variance and histogram of values are demonstrated in Fig. 5(a) and Fig. 5(b). In this paper, we design velocity models have up to four interfaces, i.e., two to five layers with different velocity values. In order to obtain a more recognizable pattern on observation data, the interfaces are kept away from the top ten grids and mainly distributed in the middle, as illustrated in Fig. 5(c).

Seismic data is generated through numerical simulation of seismic wave propagation on velocity models. In seismic exploration, a series of seismic sources and receivers are set on the ground surface to excite and record seismic wave respectively. Usually, the recorded signal will contain various types of waves such as reflected waves, diffracted waves, etc. Normally, the primary reflected wave is the main signal used to extract information regarding underground structures. In the numerical generation of seismic data in this paper, the velocity model is of grid size 100×100 , and 20 seismic sources are set on the surface uniformly with five grids interval while 100 receivers are set on every grid of the surface. Typically, acoustic wave equation (Eq. 8) is considered as the governing physics controlling the seismic wavefield changes in time.

$$\frac{\partial^2 p}{\partial t^2} - v^2 \left(\frac{\partial^2 p}{\partial x^2} + \frac{\partial^2 p}{\partial y^2} \right) = 0. \quad (8)$$

Here, p denotes pressure, i.e., the acoustic wavefield, v denotes wave velocity of the media, x and y are spatial coordinates, and t is time. Based on pseudo spectral method [45]–[47], seismic wave propagation in an arbitrary velocity model can be simulated accurately (see wavefield snapshots in Fig. 6).

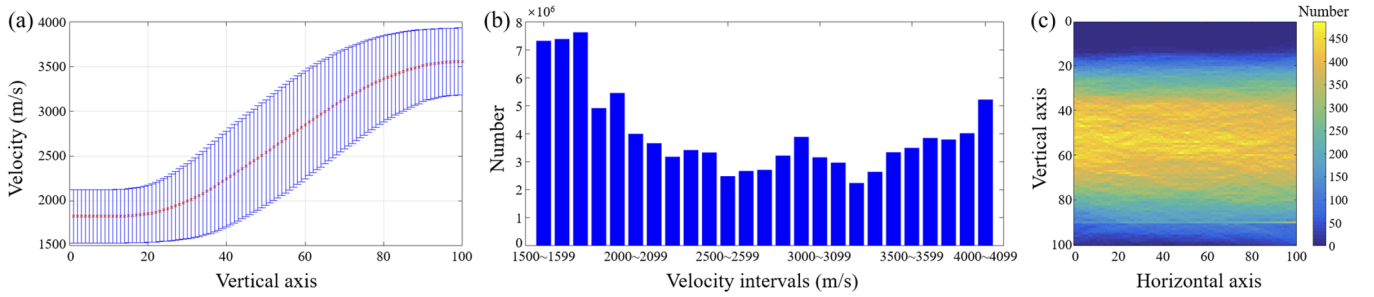


Fig. 5. The overall statistics on the training dataset. (a) The velocity distribution with respect to the depth. The red stars denote mean of velocities distributed in depth indicated on the Vertical axis, and blue intervals represent the corresponding standard deviation. (b) The histogram of values in velocity models. The blue bars denote the number of grids with velocity value in the corresponding velocity interval. (c) The interface distribution on velocity models. The number of interfaces in each grid is visualized with the right-side colormap.

The wavefield at every receiver point and every time step are saved as seismic data (such as right two figures in Fig. 3).

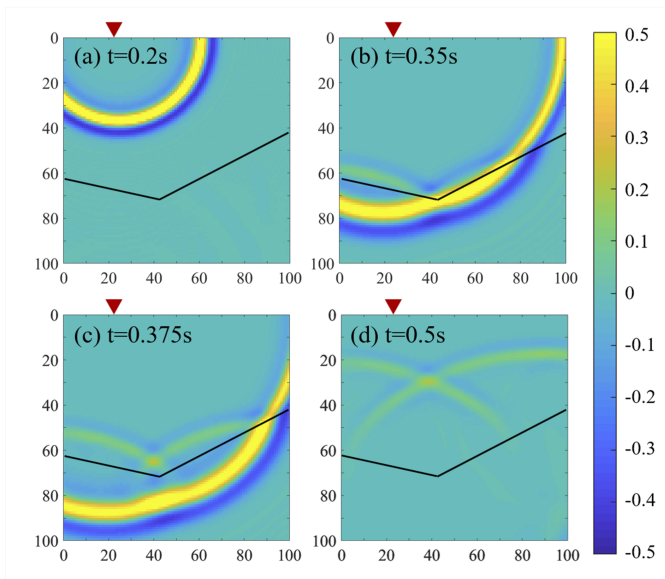


Fig. 6. Wavefield snapshots at time step (a) $t=0.2s$, (b) $t=0.35s$, (c) $t=0.375s$ and (d) $t=0.5s$. The red inverted triangle denotes the position of the seismic source where the seismic wave is excited at $t=0$. At time $t=0.35s$, the seismic wavefield firstly meets the downward interface and a small part of it reflects back. At time $t=0.375s$, a small part of the seismic wavefield reflects back on the upward interface.

Note that, the first recorded wave, which has the biggest amplitude, is called direct wave (as illustrated in Fig. 3). It represents waves that travel directly from seismic sources to the receivers, so it does not contain any information about underground structures. Below the direct wave lies the primary reflected waves, which are denoted as red and brown lines in Fig. 3. They have a much smaller amplitude since part of the wave energy will go through the interface and continue to travel in the next medium. Even in the same medium, with time goes by, the amplitude of seismic record will gradually decrease caused by dispersion and dissipation. This wavefield attenuation nature will pose a great challenge, especially for the CNNs that share uniform weights over the whole spatial dimensions.

B. Experimental Settings

We randomly divide our SeisInv dataset into three sets that 10,000 for training, 1,000 for validation and 1,000 for test. To reduce the computation complexity and for the convenience of comparing with other methods, we only utilize the data of the front 1,000 time steps and sample the data recorded by 32 receivers from the total 100 receivers uniformly. Consequently, D^i is of size $[20, 1000, 32]$ and V^i is of $[100, 100]$. We apply *MSSIM* with five different scales from window size of 11 at the beginning, and the weight for each scale is set up identical with [44]. To optimize our SeisInvNet and baseline model, we use Adam optimizer [48] with batchsize 12 and set initial learning rate as $5e-5$ following "poly" learning rate policy. During training, we carry out 200 epochs in total and set the dropout rate to 0.2 in our Velocity Model Decoder. The longest path in our SeisInvNet has 24 layers (each layer is a combination of convolution or fully connected operation, activation operation and norm operation.). Our SeisInvNet has about 10M parameters and could be trained end-to-end without any pre-processing and post-processing. Following the convention, we save the parameters that perform best on the validation set and carry out experiments on validation and test sets.

C. Baseline models

To verify the effectiveness of our SeisInvNet, we use fully convolutional networks as our baseline model. To be specific, we design the baseline model based on Encoder-Decoder Networks as ones used in [32]. The baseline model has 21 layers which are little fewer than our SeisInvNet. However, the amount of parameter in the baseline model is about 40M in our implementation that three times larger than SeisInvNet, because of frequently using convolution with large channels. To be fair, our SeisInvNet and baseline model are designed with the same basic network blocks, and trained with the same hyper parameters and optimizer mentioned in Sec. IV-B. Please refer supplementary for the detailed architecture of SeisInvNet and baseline model.

During comparison, we tested several variants of SeisInvNet and baseline model by modifying loss function configuration. For each pair comparison of SeisInvNet and baseline model, all the set up are identical. For example, in Tab. I, instead of

comparing SeisInvNet and baseline model with loss defined in Eq. 7, we also make comparisons with only L_1 loss and L_2 loss. It's worth to note that InversionNet [32] is a specific form of the baseline model that with L_1 loss, initial learning rate as $5e-4$ and learning rate policy of decreasing ten times after every 15 training epochs. In our implementation, InversionNet may not converge to its optimal because of this dramatic learning rate decreasing. All the variants are trained, validated and tested on the machine of a single NVIDIA TITAN Xp, with similar average inference time of $0.013 \pm 0.002s$.

For convenience, we use a series of Greek letter to denote each variant of SeisInvNet and baseline model that (α) for InversionNet, (β) for baseline with L_1 loss, (γ) for SeisInvNet with L_1 loss, (δ) for baseline with L_2 loss, (ϵ) for SeisInvNet with L_2 loss, (ζ) for baseline with L_2 and $MSSIM$ loss and (η) for SeisInvNet with L_2 and $MSSIM$ loss.

D. Qualitative Comparison

In this subsection, we will show some examples to visually demonstrate the inversion effects of our SeisInvNet (η) and the baseline model (ζ). In general, both methods can successfully invert the velocity model, while SeisInvNet presents more accurate value and detailed interface structures than the baseline model. From each type of velocity model in validation and test sets, we randomly select one example for comparison in Fig. 7. The examples arranged from left to right are the corresponding ground truth, SeisInvNet results, baseline model results, and the vertical velocity profiles, respectively.

The misfit degree of geological interface and velocity value are two major factors considered in evaluation. As we can see in Fig. 7, all four examples inverted by both SeisInvNet and baseline model present relatively uniform and accurate velocity distribution within every subsurface layers. Overall observation indicates that the velocity model reconstructed by SeisInvNet is more closed to the ground truth from the aspects of velocity value, subsurface structure and geological interface. To further analyze the inversion effects, we look closer at the interfaces and compare the inversion results in a pixel level. Generally speaking, the Baseline model tends to present blurred interfaces while our SeisInvNet generates a more accurate description of the interfaces, especially when the interfaces have some small undulations. Taking the example on the third row as an instance, our SeisInvNet successfully reconstructs the small bump (marked by red circle) on the second interface while baseline model totally missed this structure and presented a flat interface. Besides, the results of baseline model in the third and fourth row have a poor inversion effect with anomalous velocity area (the red rectangles in Fig. 7) and blurry interface respectively, while the results of SeisInvNet are more matched with the ground truth. A possible reason is that the baseline model vanishes spatial dimension while our SeisInvNet preserves spatial information, as discussed in Sec. IV-F.

From the velocity profiles at the vertical central axis shown in Fig. 7, we could find that our SeisInvNet is better at the velocity recovery than the baseline model. In shallow layers, the reconstructed velocity model by SeisInvNet seems

identical with the ground truth while the baseline model produces certain errors sometimes. As for the deeper layers, both methods show some discrepancy regarding to the ground truth while the error by SeisInvNet is obviously smaller. This pattern is in line with the common sense of geophysical exploration that the deeper the underground structure is, the harder it is to estimate. Moreover, the velocity jump in outputs of SeisInvNet seems more "vertical" than that in Baseline model, which means interfaces predicted by SeisInvNet are more sharper.

For further comparing inversion effect with other baseline models, we display more examples randomly selected from the test set in Fig. 8. Apparently, our SeisInvNet (η) can provide the best performance in most cases. Check supplementary materials for more results.

E. Quantitative Comparison

In this subsection, we quantitatively evaluate and compare the overall inversion effects of our SeisInvNet and baseline model via a series of metrics.

1) *Metrics*: Metrics we used are listed in the following.

a) *MAE and MSE*: We quantify the misfit error of both inversion results based on the prevalent used mean absolute error (*MAE*) and mean square error (*MSE*).

b) *SSIM and MSSIM*: We measure how well the local structures are fit by *SSIM* [40] and *MSSIM* [44].

c) *Soft F_β* : As stated previously, the quality of geological interfaces is one major factor considered when evaluating the inversion results. Geological interfaces appear as edges between two adjacent layers. Thus we can first detect edges in reconstructed velocity model and ground truth, then use evaluation method for edge detection to measure their alignment. Namely, we measure the quality of geological interfaces by evaluating the accuracy of edges after applying same edge detection method where we treat edges of \bar{V} as predicted edges and edges of corresponding V as ground truth edges.

F_β also called F-measure is a metric to measure the accuracy of classification, which is defined as

$$F_\beta = (1 + \beta^2) \cdot \frac{Precision \cdot Recall}{\beta^2 \cdot Precision + Recall}, \quad (9)$$

and can also be used to measure the accuracy of edges, it ranges from 0 to 1 with the rule of the larger the better that 1 for complete alignment and 0 reversely. However, this metric is too rigid that no matter how much predicted edges deviated from ground truth edges, it will result in a total misalignment. This problem also exists in other metrics such as *MAE* and *Cross Entropy*.

Consequently, we modify F_β to a soft metric for edge detection that more spatial closed the prediction to the target, more larger the F_β will be, see definition in Alg. 1. It's worth to note that since *Soft F_β* no longer follows its original formulation, the value range will change. In our experiments the value range may exceed 1 but still follow the original rule. We set ω to 7 and β to 1 in the following experiments.

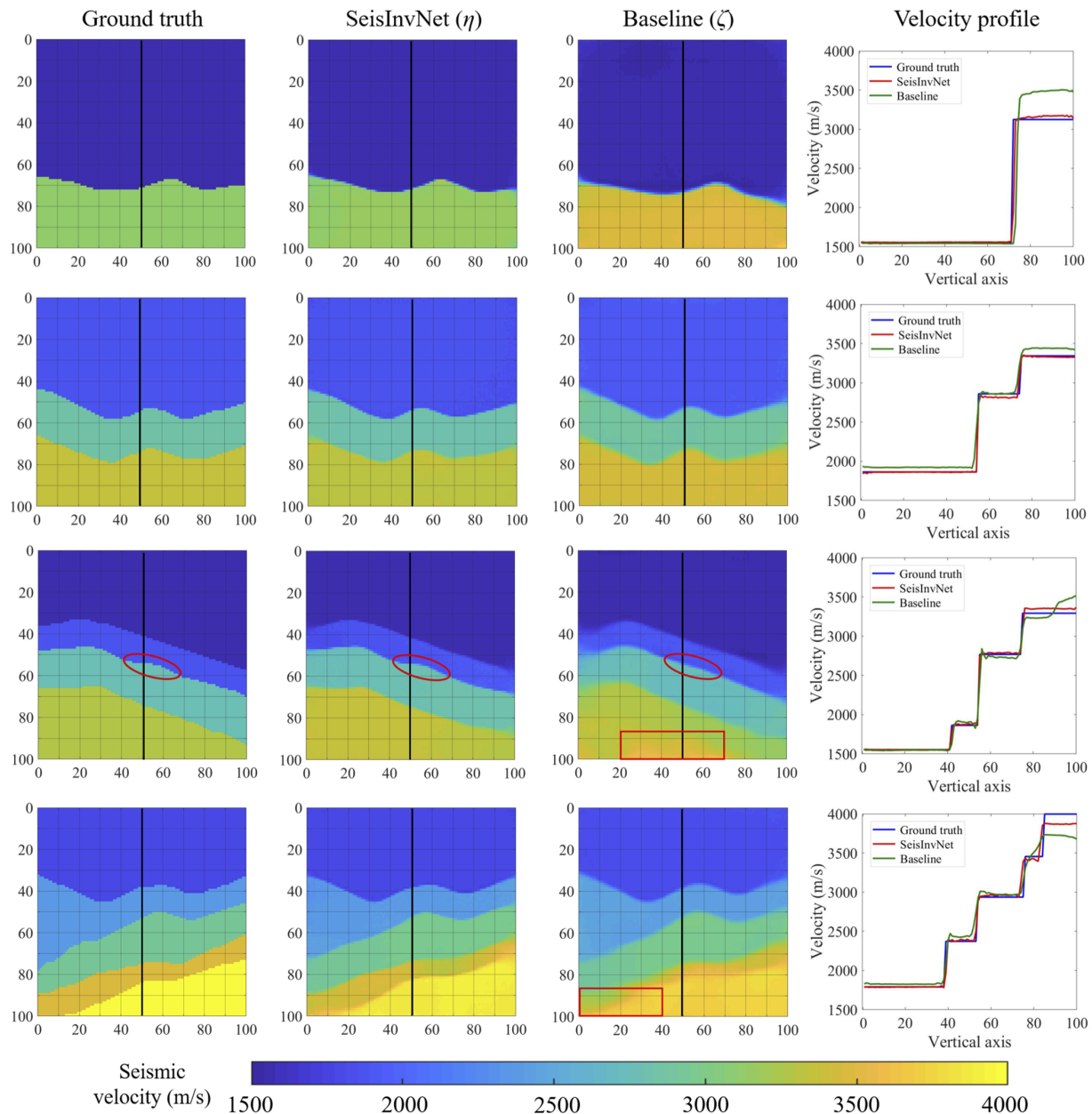


Fig. 7. Inversion results of our SeisInvNet (the second column) and Baselines (the third column) as well as Ground truth (the first column) from the validation and test sets. Vertical velocity profile at the black line is shown in the rightmost column for comparing the inverted velocity values. Each row from top to bottom exhibits examples from the velocity type I \sim IV, respectively. The red ellipses on the third row circled a small bump in the velocity model and the corresponding inversion results and the red rectangles on the third and fourth rows denote anomalous velocity areas. The comparison in this figure indicates that our SeisInvNet (η) delivers better performance than the baseline model (ζ) does.

2) *Results and Ablation Study*: The comparison results of all seven variants of SeisInvNet and baseline model, by total five metrics on both validation (valid) and test sets are listed in Tab. I. Obviously, for each pair of SeisInvNet and Baseline with same loss function configuration, our SeisInvNet show consistent superiority according to all the metrics. On the whole, our SeisInvNet (η) with L_2 and $MSSIM$ loss achieved the best performance. Since, MAE & MSE , $SSIM$ & $MMSIM$, and $Soft F_\beta$ measure the fit of velocity value, subsurface structure and geological interface respectively. Thus results of our SeisInvNet (η) should have overall the best quality on these aspects, see Fig. 7, Fig.8 or supplementary for visual results.

Besides, we show the loss curve of Baseline ζ and SeisInvNet (η) in Fig. 9. As can be seen, both methods converged quickly without overfitting on both training and validation sets, but our SeisInvNet (η) converged more rapidly and more stably, which means SeisInvNet (η) could cope this task without too much burden and may well apply to other more complex data. It's worthwhile to mention again that our SeisInvNet achieves this promising performance only with one quarter of the parameters used in the baseline model, which further proves ours' efficiency.

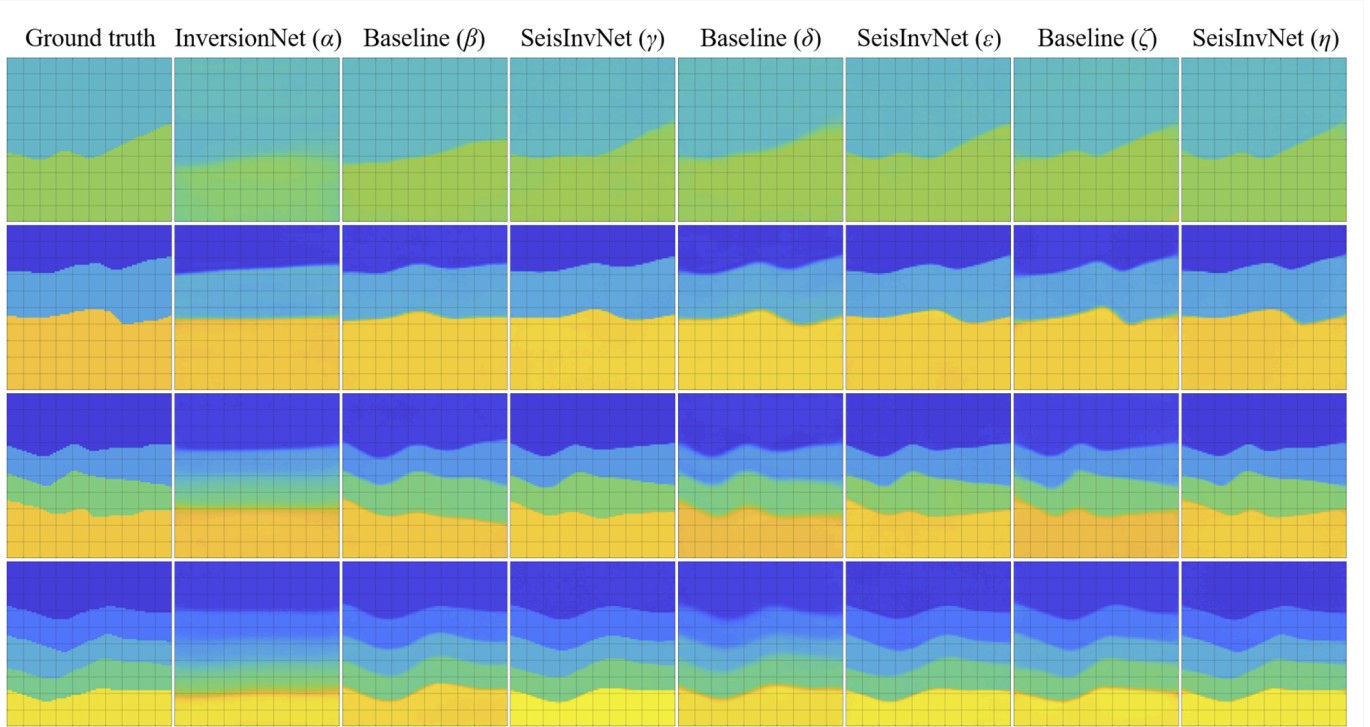


Fig. 8. Randomly selected results of all methods from the test dataset. Each row from top to bottom exhibits examples from the velocity type I ~ IV, respectively.

TABLE I

PERFORMANCE STATISTICS OF DIFFERENT METHODS ON THE FIVE METRICS AND THE TWO DATASETS. FOR EACH SET AND METRIC, THE TOP THREE RESULTS ARE HIGHLIGHTED IN RED, BLUE AND GREEN, RESPECTIVELY. THE \uparrow INDICATES THE LARGER VALUE ACHIEVED, THE BETTER PERFORMANCE IS, WHILE \downarrow INDICATES THE SMALLER, THE BETTER.

Dataset	Metric	InversionNet (α)	L_1 Loss		L_2 Loss		L_2 & $MSSIM$	
			Baseline (β)	SeisInvNet (γ)	Baseline (δ)	SeisInvNet (ϵ)	Baseline (ζ)	SeisInvNet (η)
Valid	$MAE \downarrow$	0.039207	0.028016	0.013614	0.028571	0.014404	0.027016	0.014782
	$MSE \downarrow$	0.005172	0.003578	0.001726	0.002772	0.001315	0.002539	0.001254
	$SSIM \uparrow$	0.823177	0.870728	0.932215	0.887269	0.941135	0.914004	0.953491
	$MSSIM \uparrow$	0.879223	0.93565	0.974569	0.949324	0.979259	0.969629	0.986109
	$Soft F_\beta \uparrow$	0.382764	0.566493	0.735308	0.617445	0.741195	0.671889	0.762558
Test	$MAE \downarrow$	0.039713	0.027841	0.013625	0.028504	0.01437	0.027404	0.014962
	$MSE \downarrow$	0.005234	0.00341	0.001702	0.002675	0.001272	0.002466	0.001226
	$SSIM \uparrow$	0.824075	0.870953	0.931366	0.888029	0.941919	0.914169	0.95338
	$MSSIM \uparrow$	0.878726	0.936208	0.97468	0.948736	0.979546	0.969744	0.9861
	$Soft F_\beta \uparrow$	0.383811	0.56627	0.727225	0.610375	0.741908	0.668579	0.761035

F. Mechanism Study

As stated in previous sections, the benefit of extracting spatially aligned feature map from enhanced seismic traces lies in taking full advantage of knowledge inherent in each seismic trace. Typically, feature map from different enhanced seismic trace will have different sensitivity region that each feature map would reflect knowledge focus on the different part of velocity model. In Fig. 10 we illustrate how spatially aligned features \mathbf{F}^i of SeisInvNet (η) look like. Since D^i is of size $[20, 1000, 32]$, so we will have 640 recorded seismic

traces and thus generate 640 feature maps. To save space, we only show the 32 feature maps for the 11-th seismic source (the middle seismic source). Moreover, to visualize from an overall perspective, for each feature map, we compute its average over all the 1,000 validation data, then group and further average every eight feature maps to better explore the pattern.

Easy to see from Fig. 10, feature map from recorded data by left receivers ($\# 1 \sim 8$) has high activation on the left side which means it can provide more information to reconstruct left part of velocity model. Similarly, feature maps by middle-

Algorithm 1 *Soft F_β* **Require:**

- (a) Reconstructed velocity model \bar{V} ,
- (b) Ground-truth velocity model V ,
- (c) Binarized edge detection method E .

Steps:

- 1: Compute binarized edges for both \bar{V} and V that $\bar{e} = E(\bar{V})$ and $e = E(V)$,
- 2: Smooth \bar{e} by Gaussian kernel ω that $\hat{e} = \omega * \bar{e}$, and $*$ represents convolution filter,
- 3: *Soft Precision* = $|\hat{e} \odot e|/|\bar{e}|$, \odot is Hadamard product,
- 4: *Soft Recall* = $|\hat{e} \odot e|/|e|$, \odot is Hadamard product.

Soft F_β :

Substitute *Precision* and *Recall* with *Soft Precision* and *Soft Recall* in Eq. 9, we get *Soft F_β* .

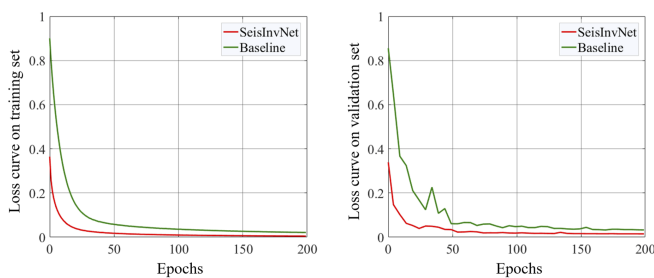


Fig. 9. Loss curves for Baseline (ζ) and SeisInvNet (η) on training and validation set.

left receivers (# 9 ~ 16), middle-right receivers (# 17 ~ 24) and right receivers (# 25 ~ 32) own information to reconstruct middle-left, middle-right and right part of velocity model, respectively. However, there is little response to the bottom part of velocity model in both feature maps, which means it's hard to infer information from seismic data to reconstruct bottom part, and implies the sensitivity region of feature maps cannot cover the whole velocity model.

Yet most results of our SeisInvNet (η) look as good as Fig. 7, so we suspect our inversion results for bottom part of velocity model may more depend on the context and the statistics information of dataset that SeisInvNet captured and memorized. The utilization of context and statistics is the primary advantage of DNNs based methods, but in the task of geophysical inversion, inversion for bottom part in velocity model by DNNs maybe still unstable and have bigger error due to the lack of direct knowledge. To be sure, the bottom part is inherent difficult to inverse as determined by the seismic inversion mechanism.

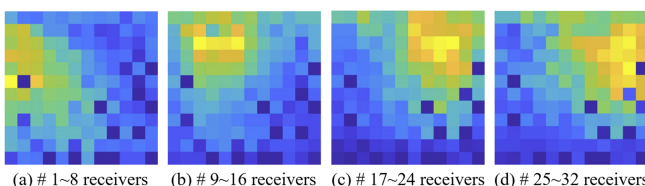


Fig. 10. Feature map visualization. We visualize feature maps follow the approach described in Sec. IV-F, each feature map is amplified for better illustration. Feature maps show clear sensitivity regions (the yellow areas).

We study and verify this potential problem via Fig. 11, which illustrates the velocity difference and variance in different layers of velocity model in the validation set, for the seven methods described in Sec. IV-C. The velocity difference is defined as mean estimated velocity minus the mean true velocity within the area determined by each layer of true velocity model. In the same manner, velocity variance measures squared deviation from mean estimated velocity can be calculated. From velocity difference in Fig. 11, we can conclude that all the seven methods tend to generate higher velocity values for shallow layers and lower velocity values for deeper layers. As for velocity variance, the bars corresponding to the top and bottom layers have lower height than the bars corresponding to the middle layers, which indicates a stable and uniform velocity distribution within the top and bottom layers. In general, variants of SeisInvNet present results with smaller velocity difference and variance within each layer, so that they could give more accurate, stable and uniform seismic inversion results. Similar observation can also be made in the test set. We have not fully understood the mechanism behind these phenomena, which may become a potential research focus in the future.

V. CONCLUSION

In this work, we dig into the problem of deep learning based seismic inversion. We found that most existing approaches could not take full advantage of seismic data and may introduce artificials. In light of these drawbacks, we analyze the intrinsic characteristics of this task and propose an end-to-end DNNs called SeisInvNet. Our SeisInvNet generates spatially aligned features from every enhanced seismic trace, which enforce every seismic trace to contribute to the reconstruction of the whole velocity model. In our experiments, these spatially aligned features actually show spatial correspondence to the velocity model, thus paving the way for subsequent components to regress velocity value by convolution operation directly.

We apply L_2 and $MSSIM$ loss together to guide SeisInvNet reconstruct velocity model considering individual position and local structures together so as to generate results closer to the target. We propose to do evaluation from the aspects of velocity value, subsurface structure and geological interface, and consequently choose five relevant metrics. Among these metrics, the proposed *Soft F_{beta}* is a relaxed version of *F-measure* that can better measure the alignment of interfaces. To train, validate and test our SeisInvNet, we collect SeisInv dataset that contains 12,000 pairs of seismic data and velocity model.

In experiments, Our SeisInvNet demonstrates superior performance against all the baseline models on SeisInv dataset by five metrics, consistently. With fewer parameters, our SeisInvNet achieves lower loss and converges more quickly and stably. From the visual comparison, our inversion results also show better quality than baseline models. In mechanism study, we further provide the evidence to verify our statements and find some potential problems to tackle in the future.

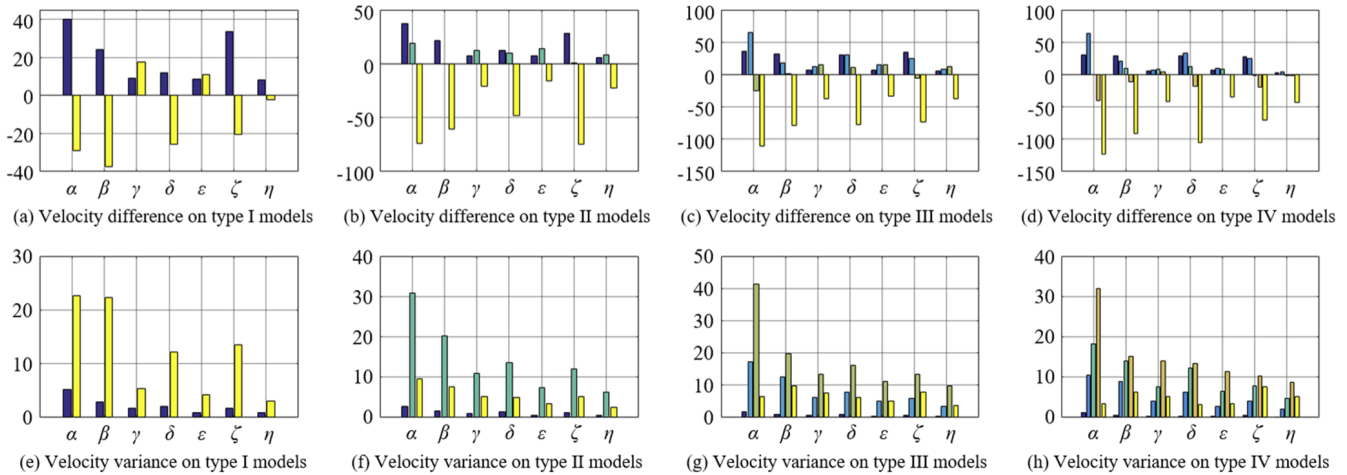


Fig. 11. Velocity difference (a) ~ (d) and velocity variance (e) ~ (h). From left to right, we show the results for velocity model of four types I ~ IV, respectively. In each subfigure, we have seven groups of bars for seven methods (α ~ (η)) respectively. For each group, bars from left to right corresponds to the layer from top to bottom.

VI. ACKNOWLEDGMENTS

This work was supported by the grants of National Natural Science Foundation of China (No. 51739007, 61702301, 51809155), the Royal Academy of Engineering under the UK-China Industry Academia Partnership Programme scheme (UK-CIAPP\314), the Key Research and Development Plan of Shandong Province (No. 2016ZDJS02A01), and Fundamental Research Funds of Shandong University.

REFERENCES

- [1] B. Biondi and A. Almomin, "Simultaneous inversion of full data bandwidth by tomographic full-waveform inversion," *Geophysics*, vol. 79, no. 3, pp. WA129–WA140, 2014.
- [2] Z. Wu and T. Alkhalifah, "Simultaneous inversion of the background velocity and the perturbation in full-waveform inversion," *Geophysics*, vol. 80, no. 6, pp. R317–R329, 2015.
- [3] R. Davy, J. V. Morgan, T. Minshull, G. Bayrakci, J. Bull, D. Klaeschen, T. Reston, D. S. Sawyer, G. Lymer, and D. Cresswell, "Resolving the fine-scale velocity structure of continental hyperextension at the deep galicia margin using full-waveform inversion," *Geophysical Journal International*, vol. 212, no. 1, pp. 244–263, 2017.
- [4] P. Lailly and J. Bednar, "The seismic inverse problem as a sequence of before stack migrations," in *Conference on inverse scattering: theory and application*. Siam Philadelphia, PA, 1983, pp. 206–220.
- [5] A. Tarantola, "Inversion of seismic reflection data in the acoustic approximation," *Geophysics*, vol. 49, no. 8, pp. 1259–1266, 1984.
- [6] R. G. Pratt, C. Shin, and G. Hick, "Gauss-newton and full newton methods in frequency-space seismic waveform inversion," *Geophysical Journal International*, vol. 133, no. 2, pp. 341–362, 1998.
- [7] J. Tromp, C. Tape, and Q. Liu, "Seismic tomography, adjoint methods, time reversal and banana-doughnut kernels," *Geophysical Journal International*, vol. 160, no. 1, pp. 195–216, 2005.
- [8] R.-E. Plessix, "A review of the adjoint-state method for computing the gradient of a functional with geophysical applications," *Geophysical Journal International*, vol. 167, no. 2, pp. 495–503, 2006.
- [9] C. Bunks, F. M. Saleck, S. Zaleski, and G. Chavent, "Multiscale seismic waveform inversion," *Geophysics*, vol. 60, no. 5, pp. 1457–1473, 1995.
- [10] R. G. Pratt, "Seismic waveform inversion in the frequency domain, part 1: Theory and verification in a physical scale model," *Geophysics*, vol. 64, no. 3, pp. 888–901, 1999.
- [11] L. Sirgue and R. G. Pratt, "Efficient waveform inversion and imaging: A strategy for selecting temporal frequencies," *Geophysics*, vol. 69, no. 1, pp. 231–248, 2004.
- [12] S. Operto and A. Miniussi, "On the role of density and attenuation in three-dimensional multiparameter viscoacoustic vti frequency-domain fwi: an obc case study from the north sea," *Geophysical Journal International*, vol. 213, no. 3, pp. 2037–2059, 2018.
- [13] C. Shin and Y. H. Cha, "Waveform inversion in the laplace domain," *Geophysical Journal International*, vol. 173, no. 3, pp. 922–931, 2008.
- [14] E. Bozdag, J. Trampert, and J. Tromp, "Misfit functions for full waveform inversion based on instantaneous phase and envelope measurements," *Geophysical Journal International*, vol. 185, no. 2, pp. 845–870, 2011.
- [15] Y. LeCun, Y. Bengio, and G. E. Hinton, "Deep learning," *Nature*, vol. 521, no. 7553, pp. 436–444, 2015.
- [16] P. Jiang, F. Gu, Y. Wang, C. Tu, and B. Chen, "Difnet: Semantic segmentation by diffusion networks," in *Advances in Neural Information Processing Systems 31*. Curran Associates, Inc., 2018.
- [17] T.-C. Wang, M.-Y. Liu, J.-Y. Zhu, A. Tao, J. Kautz, and B. Catanzaro, "High-resolution image synthesis and semantic manipulation with conditional gans," in *Proceedings of the IEEE Conference on Computer Vision and Pattern Recognition*, 2018.
- [18] O. Vinyals, A. Toshev, S. Bengio, and D. Erhan, "Show and tell: A neural image caption generator," in *The IEEE Conference on Computer Vision and Pattern Recognition (CVPR)*, June 2015.
- [19] T. Xu, P. Zhang, Q. Huang, H. Zhang, Z. Gan, X. Huang, and X. He, "AttnGAN: Fine-grained text to image generation with attentional generative adversarial networks," in *The IEEE Conference on Computer Vision and Pattern Recognition (CVPR)*, 2018.
- [20] J.-Y. Zhu, T. Park, P. Isola, and A. A. Efros, "Unpaired image-to-image translation using cycle-consistent adversarial networks," in *Computer Vision (ICCV), 2017 IEEE International Conference on*, 2017.
- [21] Z. Yi, H. Zhang, P. Tan, and M. Gong, "DualGAN: Unsupervised dual learning for image-to-image translation," in *The IEEE International Conference on Computer Vision (ICCV)*, Oct 2017.
- [22] C. B. Choy, D. Xu, J. Gwak, K. Chen, and S. Savarese, "3d-r2n2: A unified approach for single and multi-view 3d object reconstruction," in *Proceedings of the European Conference on Computer Vision (ECCV)*, 2016.
- [23] K. H. Jin, M. T. McCann, E. Froustey, and M. Unser, "Deep convolutional neural network for inverse problems in imaging," *IEEE Transactions on Image Processing*, vol. 26, no. 9, pp. 4509–4522, 2017.
- [24] C. Dong, C. C. Loy, K. He, and X. Tang, "Image super-resolution using deep convolutional networks," *IEEE transactions on pattern analysis and machine intelligence*, vol. 38, no. 2, pp. 295–307, 2016.
- [25] D. Liu, Z. Wang, B. Wen, J. Yang, W. Han, and T. S. Huang, "Robust single image super-resolution via deep networks with sparse prior," *IEEE Transactions on Image Processing*, vol. 25, no. 7, pp. 3194–3207, 2016.
- [26] Y. Wang, F. Liu, K. Zhang, G. Hou, Z. Sun, and T. Tan, "Lfnet: A novel bidirectional recurrent convolutional neural network for light-field image super-resolution," *IEEE Transactions on Image Processing*, vol. 27, no. 9, pp. 4274–4286, 2018.

- [27] T.-C. Wang, M.-Y. Liu, J.-Y. Zhu, G. Liu, A. Tao, J. Kautz, and B. Catanzaro, "Video-to-video synthesis," *arXiv preprint arXiv:1808.06601*, 2018.
- [28] M. Zhang, R. Wang, X. Gao, J. Li, and D. Tao, "Dual-transfer face sketch-photo synthesis," *IEEE Transactions on Image Processing*, vol. 28, no. 2, pp. 642–657, 2019.
- [29] B. Moseley, A. Markham, and T. Nissen-Meyer, "Fast approximate simulation of seismic waves with deep learning," *arXiv:1807.06873*, 2018.
- [30] A. van den Oord, S. Dieleman, H. Zen, K. Simonyan, O. Vinyals, A. Graves, N. Kalchbrenner, A. W. Senior, and K. Kavukcuoglu, "Wavenet: A generative model for raw audio," *arXiv preprint arXiv:1609.03499*, 2016.
- [31] M. Araya-Polo, J. Jennings, A. Adler, and T. Dahlke, "Deep-learning tomography," *The Leading Edge*, vol. 37, no. 1, pp. 58–66, 2018.
- [32] Y. Wu, Y. Lin, and Z. Zhou, "Inversionnet: Accurate and efficient seismic waveform inversion with convolutional neural networks," in *SEG Technical Program Expanded Abstracts 2018*. Society of Exploration Geophysicists, 2018, pp. 2096–2100.
- [33] T. Dahlke, M. Araya-Polo, C. Zhang, C. Frogner, and T. Poggio, "Predicting geological features in 3d seismic data," in *Advances in Neural Information Processing Systems 29, 3D Deep Learning Workshop*. Curran Associates, Inc., 2016.
- [34] Ö. Yilmaz, *Seismic data analysis: Processing, inversion, and interpretation of seismic data*. Society of exploration geophysicists, 2001.
- [35] A. B. L. Larsen, S. K. Sønderby, H. Laroche, and O. Winther, "Autoencoding beyond pixels using a learned similarity metric," in *Proceedings of the 33rd International Conference on International Conference on Machine Learning*, 2016.
- [36] Y. Taigman, A. Polyak, and L. Wolf, "Unsupervised cross-domain image generation," *International Conference on Learning Representations (ICLR)*, 2016.
- [37] O. Ronneberger, P. Fischer, and T. Brox, "U-net: Convolutional networks for biomedical image segmentation," in *Medical Image Computing and Computer-Assisted Intervention – MICCAI 2015*, 2015.
- [38] M. Araya-Polo, T. Dahlke, C. Frogner, C. Zhang, T. Poggio, and D. Hohl, "Automated fault detection without seismic processing," *The Leading Edge*, vol. 36, no. 3, pp. 208–214, 2017.
- [39] W. Wang, F. Yang, and J. Ma, "Velocity model building with a modified fully convolutional network," in *SEG Technical Program Expanded Abstracts 2018*. Society of Exploration Geophysicists, 2018, pp. 2086–2090.
- [40] Z. Wang, A. C. Bovik, H. R. Sheikh, and E. P. Simoncelli, "Image quality assessment: from error visibility to structural similarity," *IEEE Transactions on Image Processing*, vol. 13, no. 4, pp. 600–612, 2004.
- [41] Y. Lin and L. Huang, "Acoustic-and elastic-waveform inversion using a modified total-variation regularization scheme," *Geophysical Journal International*, vol. 200, no. 1, pp. 489–502, 2014.
- [42] E. M. Takam Takougang and Y. Bouzidi, "Imaging high resolution velocity and attenuation structures from walkaway vsp data in a carbonate reservoir using visco-acoustic waveform tomography," *Geophysics*, vol. 83, no. 6, pp. 1–64, 2018.
- [43] G. Landro, V. Serlenga, G. Russo, O. Amoroso, G. Festa, P. P. Bruno, M. Gresse, J. Vandemeulebrouck, and A. Zollo, "3d ultra-high resolution seismic imaging of shallow solfatara crater in campi flegrei (italy): New insights on deep hydrothermal fluid circulation processes," *Scientific Reports*, vol. 7, no. 1, p. 3412, 2017.
- [44] Z. Wang, E. P. Simoncelli, and A. C. Bovik, "Multiscale structural similarity for image quality assessment," in *The Thirty-Seventh Asilomar Conference on Signals, Systems Computers, 2003*, 2003.
- [45] D. D. Kosloff and E. Baysal, "Forward modeling by a fourier method," *Geophysics*, vol. 47, no. 10, pp. 1402–1412, 1982.
- [46] J. Virieux, H. Calandra, and R.-E. Plessix, "A review of the spectral, pseudo-spectral, finite-difference and finite-element modelling techniques for geophysical imaging," *Geophysical Prospecting*, vol. 59, no. 5, pp. 794–813, 2011.
- [47] T. Furumura, B. Kennett, and H. Takenaka, "Parallel 3-d pseudospectral simulation of seismic wave propagation," *Geophysics*, vol. 63, no. 1, pp. 279–288, 1998.
- [48] D. P. Kingma and J. Ba, "Adam: A method for stochastic optimization," *International Conference on Learning Representations (ICLR)*, 2015.